TOPICAL REVIEW

Nanospring formation—unexpected catalyst mediated growth

D N McIlroy[1]**, A Alkhateeb**[1]**, D Zhang**[1]**, D Eric Aston**[2]**,
Andrew C Marcy**[2] **and M Grant Norton**[3]

[1] Department of Physics, Engineering and Physics Bldg, University of Idaho, Moscow,
ID 83844-0903, USA
[2] Department of Chemical Engineering, University of Idaho, Moscow, ID 83844-1021, USA
[3] School of Mechanical and Materials Engineering, Washington State University, Pullman,
WA 99164-2920, USA

Abstract
Nanosprings are a new form of nanowires that have potential applications in
nanoelectronics, nanomechanics, and nanoelectromechanical systems. In this
review we will examine the growth mechanism of these novel nanostructures.
The synthesis of nanowires by the vapour–liquid–solid growth mechanism,
first proposed by Wagner and Ellis, will be explored and then extended to the
development of a model to explain the formation of nanosprings.

Contents

1. Introduction

Nanoscale materials are being touted as the wave of the future in all manner of applications ranging from electronics to pharmaceuticals. In the case of electronics, the trend towards miniaturization to the nanoscale has been predicted by Moore's law [1], which states that computing power doubles every 18 months. Moore's law essentially translates into higher transistor densities, which, in turn, drives the dimension of line features below 100 nm. It has only been in the past decade that solid state physicists have wholeheartedly embraced the concept of nanoscience. Ironically, chemists and biologists have at some level always worked at the nanoscale. This interest in nanoscience on the part of physicists has been fuelled by the repeated discoveries of unanticipated quantum confinement-induced behaviour of materials, be they electronic or optical in nature, as one or more of their dimensions (d) approaches the nanoscale ($d < 100$ nm). Nanoscience is a natural fit for solid state physicists since much of their research revolves around the development of new materials that exhibit novel properties. From a more applied standpoint, nanoscale materials allow the utilization of the principles of quantum mechanics for technological applications.

Nanoscale materials, such as nanoparticles and nanowires, are attractive research areas because they provide the opportunity to study quantum confinement-induced phenomena without the need to employ a costly apparatus. For example, monodispersed metallic [2, 3] and semiconducting [4] nanoparticles—zero-dimensional quantum structures—can be synthesized using established colloidal chemistry techniques and in some cases are commercially available (for example, Evident Technologies). The synthesis of the families of free standing one-dimensional quantum structures, nanowires and nanotubes, is typically more equipment intensive than colloidal synthesis of nanoparticles, yet typically an order of magnitude less than molecular beam epitaxy systems used in the construction of quantum well structures. The rapid growth in research in nanomaterials can be attributed, in part, to the accessibility of nanoscale materials synthesis.

Nanowires are attractive nanomaterials for a variety of reasons; however, it is their versatility that makes them so attractive from a technological standpoint. Metallic [5–7], semiconducting [8–48], and dielectric [49] nanowires, as well as more exotic perovskite nanowires [50], have been synthesized. The vast variety of different types of nanowires greatly simplify the development of nanowire-based technology. While confinement effects will need to be taken into account when designing nanowire-based electronics, the selection of the correct material for the application is greatly simplified since the bulk properties of available nanowire materials are well known. The rectifying properties of nanowire-based devices have been demonstrated with a variety of different types of material [51–56], which illustrates the versatility of nanowire-based electronic devices. In addition to the use of nanowires as components in rectifying devices, it has been shown that these nanowire-based devices can be used as biological and chemical sensors [57] and molecularly gated switches [58].

The optical applications of nanowires are slightly more complicated than nanowire electronics due to quantum confinement, which produces strong blue shifts in photoluminescence [59–63] and electroluminescence [52, 55] for appropriately small nanowire diameters of the order of 50 nm or less. In addition to size dependent shifts, the optical properties of nanowires are geometrically anisotropic, which produces polarization dependence in their optical signatures. In the case of metallic nanowires the plasmon resonance is enhanced when the incident radiation is polarized orthogonal to the nanowire axis [64]. In contrast, the photoluminescence of InP nanowires is enhanced when the illuminating radiation is polarized parallel to the nanowire axis [61]. In this system the polarization dependence has been attributed to dielectric contrast between the nanowire and the surrounding air/vacuum medium,

as opposed to quantum confinement effects. The formation of free standing III–V superlattice nanowires has also been realized [55, 65, 66], further illustrating the versatility of nanowires for producing complex structures.

An added, yet poorly understood, feature of nanowires is their propensity to form complex geometric structures. The simpler structures include *in situ* biaxial [67] and coaxial nanowires [44, 68], intermediate structures consisting of nanowires and nanocrystals/particles [34, 35, 37, 39, 69], and highly complex three-dimensional helically shaped nanowires in the form of quasi-nanosprings [69], amorphous nanosprings [70], and helical crystalline core nanowires [71]. These complex helical nanowires could be of vast importance to the development of novel nanowire-based technology in the form of accelerometers, sensors, and mechanical actuators.

This review will address the formation of linear and helical nanowire structures, which we will refer to from this point on as nanosprings, that grow *via* the vapour–liquid–solid (VLS) growth mechanism first proposed for whisker formation by Wagner and Ellis [72]. The rationale behind the inclusion of linear nanowire formation in this review is that the VLS mechanism used to describe linear nanowire formation is the foundation upon which a model of nanospring formation has been built. It is important to note that alternative techniques for VLS growth of nanowires exist, such as solution phase/hydrothermal synthesis of nanowires. We have chosen to limit our discussion to VLS growth of nanowires because it is this mechanism that leads to the formation of nanosprings.

2. Synthesis of nanowires utilizing the vapour–liquid–solid growth mechanism

The VLS mechanism first proposed by Wagner and Ellis [72] is simplistic in nature, yet is subtly complex. The VLS model is most readily grasped pictorially. Figure 1 is a schematic representation of nanowire formation by the VLS mechanism. The key feature is a liquid catalyst that is able to absorb material from the surrounding vapour. If the catalyst is not liquid, material in the vapour will not be absorbed, thereby prohibiting nanowire formation. Under the appropriate conditions of temperature and vapour pressure, the liquid will absorb material from the vapour phase introduced either in elemental form or as a molecular precursor. In the chemical vapour deposition process, a molecular precursor is used [39, 41, 70]. As the catalyst absorbs more and more material it eventually becomes supersaturated, at which point material is deposited at the catalyst–substrate interface (figure 1(b)), thereby establishing nanowire formation (figure 1(c)). Extended formation of the nanowire can be maintained as long as a sufficient quantity of reactant is present and the temperature of the catalyst is above the melting point. If either of these conditions is not met, nanowire formation will cease. From the above description of the VLS mechanism, it is clear that the catalyst dictates whether or not nanowire formation will occur.

2.1. The catalyst

2.1.1. The alloying and solubility of materials with the catalyst. In order to synthesize nanowires utilizing the VLS mechanism, an appropriate choice of catalyst must be made. The first step towards choosing the catalyst is to decide on the type of nanowire to be synthesized. The elements needed for the construction of the nanowire must be soluble in the liquid catalyst. For single-element nanowires, such as Si and Ge, it is usually sufficient to identify metals that form a eutectic phase with the element in question—an alloy that has a lower melting temperature than the pure metal. In the case of compound materials, such as boron carbide and silicon carbide, this decision is complicated because two or more
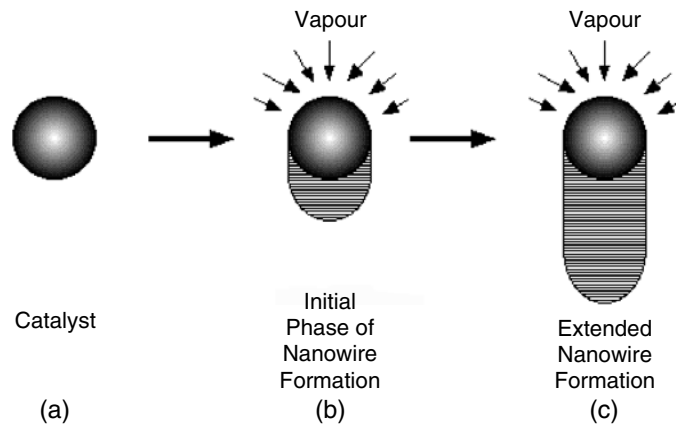
Figure 1. An illustration of the VLS growth mechanism for nanowire formation.
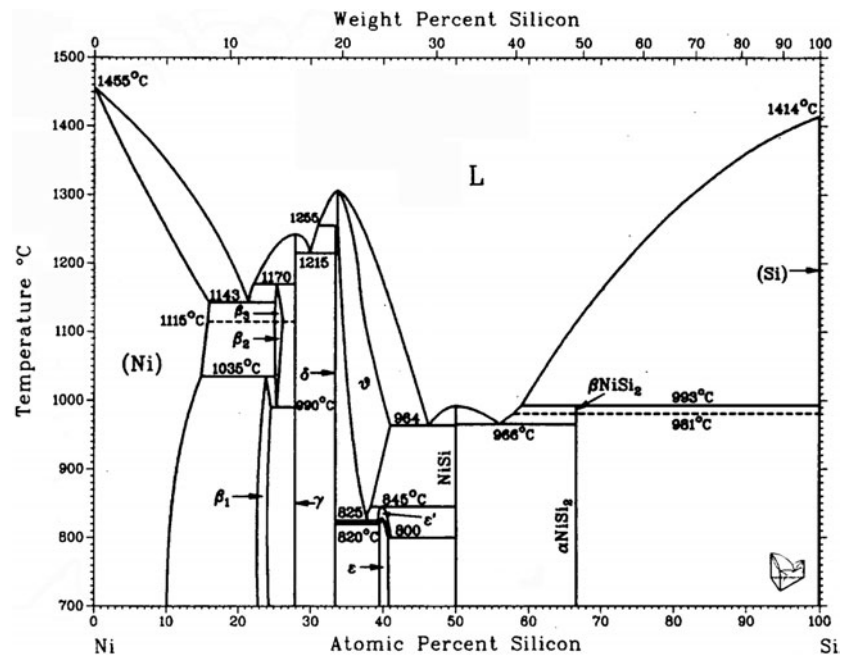

Figure 2. The phase diagram of NiSi [73].

elements need to be simultaneously absorbed by the catalyst. Typically, the best approach when attempting to synthesize a binary nanowire is to identify the alloy of the metal (catalyst) and one of the elements of the nanowire with the lowest melting temperature. An equilibrium phase diagram [73] provides invaluable information for this purpose. From the viewpoint of nanowire growth, the most important information obtained from figure 2 is the melting temperature as a function of composition. For example, a composition containing 46 at.% of Si is liquid at 964 °C—the minimum temperature for growing SiC nanowires. However, the growth temperature can be lowered if the size of the catalyst is reduced to 200 nm or less. It has been demonstrated that the melting temperature of nanoparticles is less than that of the

bulk due to their large surface area to volume ratio [74–77]. Consequently, the temperature for nanowire synthesis can be lowered by a few decades relative to the bulk melting temperature of the alloy catalyst.

In most cases pure elements have been used as catalysts for initiating nanowire growth [8, 10, 11, 13, 14, 20–23, 29, 30, 32, 33, 35, 37, 43–49]; however, we have found that eutectics can greatly simplify the synthesis of nanowires [39, 70]. Their advantages are twofold. Eutectics are much more resistant to oxidation. Secondly, because of their lower melting temperature, the initiation of nanowire formation can be achieved at significantly lower temperatures. For example, the melting temperature of pure Fe is 1535 °C, as opposed to 1174 °C for an FeB composition containing 17 at.% B [73]. Furthermore, Fe nanoparticles are readily oxidized, while we have found FeB nanoparticles to be extremely resistant to oxidation. The use of eutectics allows for the tailoring of the catalyst melting temperature. For instance, the melting temperature of NiB with 39 at.% B is 1031 °C, 12% lower than FeB. The use of NiB has enabled the synthesis of boron carbide nanowires at 960 °C, as compared to 1100–1200 °C using FeB [39, 70]. Eutectic catalysts have also been successfully used to synthesize boron nitride [12], gallium nitride [9], zinc oxide [16], and silicon carbide [78] nanowires.

An additional consequence of the choice of the catalyst is the morphology of the nanowire. Jackson and Wagner [79] found that the morphologies of micron sized whiskers were catalyst dependent. Whiskers with a hexagonal cross-section were obtained when an Au catalyst was used, but when Ni was used whiskers with both hexagonal and circular cross-sections were observed. The catalyst dependent cross-sections were explained in terms of minimization of the surface free energy of the whisker and the growth mechanism at the catalyst–whisker interface, e.g., growth rate.

2.1.2. Catalyst shape. In addition to dictating the composition of the nanowire, the catalyst also has a strong influence on the geometry of the growing nanowire, and in the case of nanosprings is the dominant factor. Therefore, a brief discussion of the types of catalyst geometry that have been experimentally observed is in order. The ramifications of catalyst geometry will be discussed in greater detail in section 4.

Figure 3 shows two transmission electron microscope (TEM) images of nanowires capped with the catalyst. The nanowire in figure 3(a) is crystalline boron carbide and the solidified catalyst is crystalline iron boride (Fe_3B). The nanowire in figure 3(b) is cubic silicon carbide and the catalyst is nickel silicide (Ni_3Si). The catalysts in figure 3 represent two types of shapes that the catalyst may exhibit, which are a consequence of a wetting or non-wetting interface between the liquid catalyst and the solid nanowire. Far less commonly observed is the silo-like, or hemispherical, shape shown in figure 3(a), which consists of a hemisphere atop a cylinder. The spherical shape of the Ni_3Si catalyst in figure 3(b) is the most common shape and probably minimizes the surface free energy. The minimum radius (r_{min}) of the catalyst and its dependence on the degree of supersaturation is given by

$$r_{min} = \frac{2\sigma_{LV} V_L}{RT \ln \sigma_{LV}} \tag{1}$$

where σ_{LV} is the liquid–vapour interfacial energy (γ_{LV}), V_L is the liquid molar volume, and R is the gas constant and T is temperature [80].

The interface between the catalyst and the nanowire falls into two classes, wetting or non-wetting, which in turn is dictated by the surface tension at the edge of the catalyst in contact with the substrate. As surface tension is a function of temperature and solute composition, it need not be constant over the entire catalyst surface during VLS growth. Figure 4 is a schematic representation of wetting and non-wetting and the corresponding surface energies
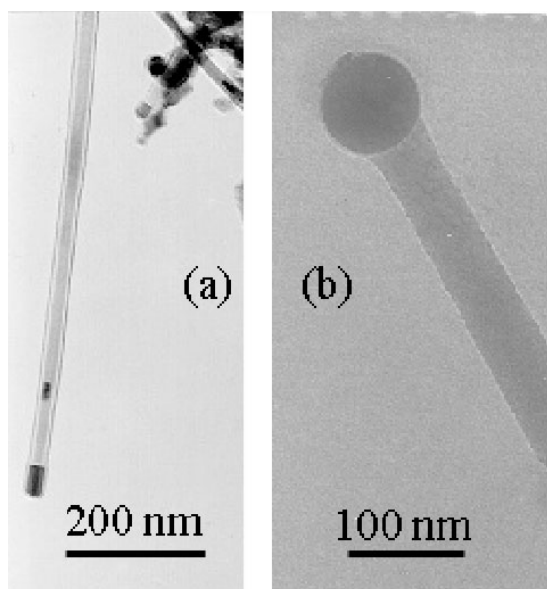
Figure 3. (a) A cylindrically/hemispherically shaped iron boride catalyst atop a boron carbide nanowire, (b) a spherically shaped nickel silicide catalyst atop a silicon carbide nanowire.
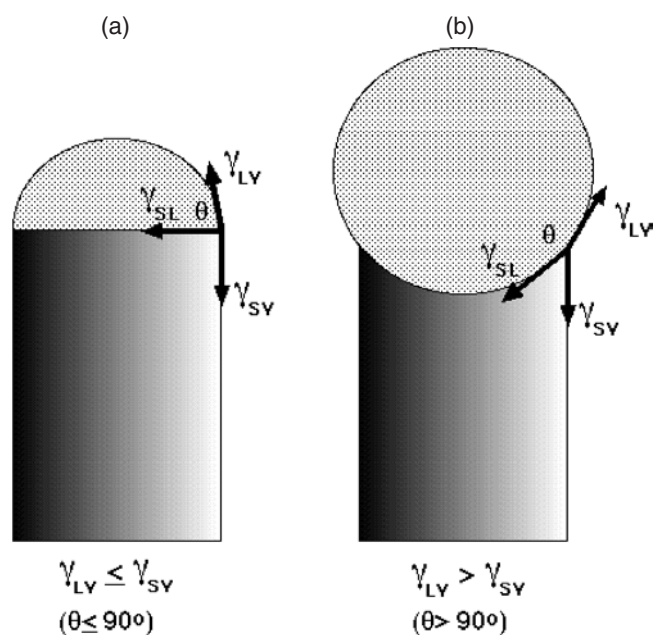
Figure 4. An illustration of the surface tensions at the catalyst nanowire interface for (a) a hemispherical catalyst and (b) a spherical catalyst.

between liquid and vapour phases (γ_{LV}), solid and liquid phases (γ_{SL}), and solid and vapour phases (γ_{SV}). The catalyst wets the nanowire if $\gamma_{LV} < \gamma_{SV}$ (figure 4(a)) and is non-wetting if $\gamma_{LV} > \gamma_{SV}$ (figure 4(b)). Consequently, it is the competition between these two surface

energies, in conjunction with γ_{SL}, which defines the geometry of the catalyst with the minimal free energy.

The diagrams in figure 4, for pinned angles of a liquid drop, represent the two physical scenarios for acute (figure 4(a)) and obtuse contacting angles (figure 4(b))—what would be respectively called wetting and nonwetting cases for thermodynamic contact angles [81]. This analogy holds for the snapshot energy diagram as long as steady-state growth is assumed within a finite window of time. The energy vectors for each interface are drawn in their corresponding planes, but only γ_{LV} and γ_{SL} are truly fixed as in the traditional Neumann triangle-like construction. (The liquid surface tension must be tangent to the drop as shown, and γ_{SV} similarly has one possible position.) It is impossible here to know or fix the physical direction of γ_{SV} for a given drop diameter because of the 'fixed edge condition'. It may truly lie anywhere between being collinear with γ_{SL} and as shown on the wire surface. Even knowing all the energy magnitudes and the apparent contact angle is not enough because internal stresses work with γ_{SV} to balance the forces in all directions, whether at steady state or equilibrium. However, since the most critical parameter is θ, the angle made by γ_{LV} and γ_{SL}, it is sufficient and logical to fix γ_{SV} at the wire surface for comparisons of relative work. What we can get from the application of the force balance is a general understanding of the physical differences between the two geometries in figure 4. From examination of figure 4(a) we can conclude that $\gamma_{LV} < \gamma_{SV}$ for the hemispherical catalyst geometry and from figure 4(b) that $\gamma_{LV} > \gamma_{SV}$ for the spherical catalyst geometry. Finally, the surface energy at the solid–liquid interface (γ_{SL}) will depend on the growth direction of the nanowire and the surface free energy (γ_{SV}) of the its sidewalls.

An added complexity of the catalyst is the dependence of γ_{LV} and γ_{SL} on composition, i.e., the dilute concentrations of the materials absorbed from the vapour. Therefore, the type of material absorbed, as well as the concentration within the catalyst, can affect the magnitudes of these surface tensions, thereby altering the geometry of the catalyst. Furthermore, the concentration gradient driving mass transfer within the droplet could cause a significant surface tension gradient, which opens up the possibility for Gibbs' elasticity and Marangoni effects contributing to complex growth behaviours. The change in interfacial energy between the solid nanowire and the liquid catalyst due to the presence of material absorbed by the catalyst can be quantified according to the Gibbs adsorption isotherm [82]:

$$\mathrm{d}\gamma_{SL} = RT \sum_i \Gamma_i \ln a_i \tag{2}$$

where Γ_i is the excess concentration at the interface and a_i is the activity of the ith species adsorbed. From examination of equation (1), we see that changes in the materials absorbed by the catalyst, or the introduction of additional elements, in conjunction with changes in temperature can introduce imbalances at the point of convergence of the three surface energies, also referred to as the three-phase interline or wetted perimeter. The ramifications of these imbalances are that the shape and mass of the catalyst may not necessarily be constant over the entire duration of nanowire formation. An example of this can be seen in figure 3(a), where a portion of the FeB catalyst has become embedded within the nanowire. The significance of the ejection of catalyst mass and the subsequent embedding of this ejected material in the nanowire will come to light when we examine nanospring formation in section 4.

One final point regarding the impact of the catalyst geometry on nanowire formation: the diameter of the catalyst can be equal to or greater than that of the nanowire but never less. A consequence of this axiom is that the diameter of the hemispherical, or silo-like, catalyst in figure 3(a) must be equal to that of the as-forming nanowire in order to satisfy the interline boundary conditions. These restrictions do not hold for the case of the spherical catalyst in figure 3(b) where its diameter exceeds that of the nanowire. When we examine the

thermodynamic work of adhesion in section 4, we will see that the wetting catalyst geometry in figure 3(a) precludes nanospring formation.

2.1.3. Catalyst preparation and application.   There are a variety of ways of preparing the catalyst and introducing it into the process; however, in the end, the synthesis process will dictate the appropriate methodology. For laser ablation synthesis of nanowires the catalyst is introduced directly into the ablation target. This is easily achieved by mixing powders of the catalyst and the nanowire material and then pressing it into a target. In the case of flow reactors, the catalyst can either be deposited onto the substrate prior to insertion into the furnace or placed in a crucible directly in the furnace, upstream from the substrate upon which nanowires will be deposited, where transport to the substrate is facilitated by the flow of a background gas. For CVD synthesis of nanowires, the catalyst is typically applied to the surface prior to nanowire synthesis. This can be done either *in situ* or *ex situ*. *In situ* application in CVD processes is achieved by first introducing a metallocene precursor, for example ferrocene ($(C_5H_5)_2Fe$), into the deposition chamber for a short period of time, thereby depositing an extremely thin metal film of the order of tens of monolayers onto the substrate. The deposition temperature for the catalyst is typically well below the nanowire synthesis temperature, but again this will depend on the choice of the precursor and the types of nanowire to be synthesized. This step is then followed by nanowire synthesis.

In the case of *ex situ* application of an elemental catalyst, a number of physical vapour deposition techniques can be utilized, such as sputtering and molecular beam epitaxy. A few to tens of monolayers of the catalyst metal are deposited onto the substrate, which is then inserted into the CVD reactor. For both of these choices the rationale for depositing a few monolayers of the catalyst is twofold. First, extremely low coverage of the catalyst material will facilitate islanding, which is critical to nanowire formation. Secondly, the amount of catalyst on the substrate will dictate the size of the metal islands, which in turn will dictate the diameter of the nanowires. The primary drawback to these two approaches is that the size distribution of the islands cannot be readily controlled.

An alternative approach to *ex situ* application of the catalyst is to produce extremely fine powders that can be suspended in a solvent and then applied to the substrate. This approach is ideally suited for the use of eutectics as the catalyst. Currently, there are a number of commercially available sources for metallic nanoparticles. In the case of more exotic eutectic materials, such as NiB or FeB, powders consisting of particles of the order of hundreds of microns must be processed to achieve nanoscale particles. The procedure utilized in our laboratory is to take the purchased powders and grind them with pestle and mortar for 10–12 h. The powder is then suspended in ethanol and sequentially passed through a series of polycarbonate membranes in decreasing order of pore size, where the final pore size is 100 nm. The end product is an ethanol solution containing suspended particles 100 nm, or less, in diameter. Prior to applying the catalyst to the substrate surface, the solution is sonicated for approximately 5 min and then left to stand for 12 h. The latter step allows the larger particles to settle out of suspension leaving only the smallest nanoparticles in solution. The end product is a nanoparticle distribution in the range of 20–100 nm. A dropper is then used to apply the solution to the substrate. The ethanol is allowed to evaporate and then the procedure is repeated until the desired concentration of nanoparticles is achieved. Rapid evaporation of the ethanol causes the nanoparticles to agglomerate in patches on the surface. This is undesirable since upon heating the small nanoparticles coalesce into larger particles, thereby producing nanowires with large diameters. An alternative method of applying the ethanol nanoparticle solution is to spin coat the solution onto the substrate.
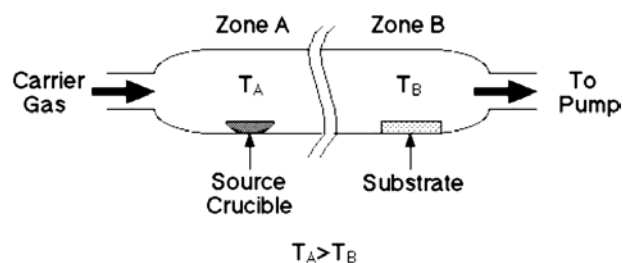
Figure 5. A schematic diagram of a flow reactor design used to synthesize nanowires.

2.2. Methods for VLS synthesis of nanowires

The VLS synthesis only requires the presence of a metallic catalyst and nanowire material in the vapour. Consequently, a broad spectrum of VLS-based techniques have been developed for synthesizing nanowires. Only the three primary techniques will be covered, namely flow reaction, laser ablation, and chemical vapour deposition (CVD), which includes plasma-enhanced chemical vapour deposition (PECVD). However, the primary focus will be on CVD-based techniques utilized in our laboratory.

2.2.1. Flow reaction formation of nanowires. The most common flow reactor consists of a quartz flow tube inside a furnace. A schematic of a flow tube is shown in figure 5. The reactor is split into temperature zones thereby establishing a temperature gradient across the flow tube. A carrier gas is introduced at the high temperature end and pumping occurs on the low temperature end. The source materials are placed in a crucible upstream (zone A) from the nanowire collection (zone B), which is maintained at a lower temperature than zone A. The temperature and pressure in zone A must be balanced such that sublimation or vaporization of the source materials is facilitated. The geometry and temperature differential of the flow reactor leads to the condensation of source materials on the substrate. The temperature in zone B must exceed the melting point of the catalyst, yet be below its sublimation or vaporization temperature.

The catalyst can be introduced either by seeding the substrate prior to insertion into the reactor or by simultaneously introducing it into the vapour with the source materials for the nanowires. In the latter case, the catalyst is either placed in zone A with the source material, mixed in with the source material, or placed in an intermediate zone. The operating temperatures and gas flow rates are dependent on the geometry of the reactor, the type of nanowire to be synthesized and the types of source material and catalyst used in the process.

The advantages of these reactors are that they are relatively inexpensive to build, versatile, simple to operate and easy to maintain. In addition, the use of solid, sublimable precursors in the form of powders simplifies the identification of optimal operating conditions for the synthesis of nanowires. A shortcoming of these systems is that oxygen contamination can be problematic. However, if judicious efforts are made to eliminate oxygen, extremely pure nanowires can be realized.

2.2.2. Laser ablation of nanowires. In some ways, laser ablation of nanowires is very similar to flow reaction synthesis. The technique is fairly straightforward. A target is constructed from powders of the materials forming the desired nanowire, as well as a metallic catalyst, also in powder form. The powders are combined in the appropriate ratios, mixed, and pressed into a solid target. In the case of Si nanowires, a Si substrate with a metallic catalyst applied to the surface suffices. The target is then placed in a vacuum vessel, which is then back-filled with

an inert gas. The purpose of the background gas is to facilitate thermalization and subsequent condensation of the catalyst, where subsequent nucleation and nanowire formation is due to absorption of materials from the surrounding vapour. Either Nd:YAG lasers [22, 37] or excimer lasers [8, 19–21, 27, 28] are typically used in these ablation processes. These two types of laser have the necessary power for ablation, although they operate at significantly different wavelengths. The primary factors for the successful laser ablation of nanowires are the choice of catalyst, the correct ratio of nanowire material and catalyst in the target, and background gas pressure.

A hybrid approach to nanowire synthesis developed by Wu *et al* [65] combines laser ablation with a flow reactor process, which has yielded superlattice nanowires of Si/SiGe. The role of the flow furnace is to produce Si nanowires, while the laser ablation process is to introduce Ge periodically into the vapour. The Ge is absorbed by the catalyst and incorporated into the forming nanowire. Through judicious control of the process, they have achieved superlattice periodicities of Si/SiGe of approximately 250 nm. The results of this study bode well for superlattice nanowire devices.

2.2.3. Chemical vapour deposition and plasma-enhanced chemical vapour deposition of nanowires. The primary distinction between CVD processes for VLS synthesis of nanowires and the proceeding processes is that the precursor materials are either gases or vapours. The term CVD is very generic and therefore encompasses many variants of the same theme. Consequently, a flow reactor could be used as intended or modified to operate as a CVD reactor. Along these lines, a CVD system could be combined with laser ablation, similar to the system used by Wu *et al* [65] to grow superlattice nanowires. The construction of a CVD system is fairly simple and straightforward. In fact, the basic reactor is very similar to a flow reactor. What sets CVD apart from a flow reactor is gas handling. In CVD, the only requirement of the precursor is that it be a vapour upon introduction into the reactor. Therefore, gases, liquids and sublimable solids are all candidates as CVD precursors. Gaseous precursors are by and large the simplest of the three for use in CVD since their introduction into the reactor can be readily metered with mass flow control valve technology.

The use of liquid precursors is more involved than gases but still very manageable. Typically, an inert gas (carrier gas) such as Ar or N_2 is bubbled through a vessel containing the liquid precursor, often referred to as a bubbler. Through judicious control of the liquid temperature and carrier gas flow rate, the concentration of the precursor in the gas–vapour mixture can be metered with a high degree of precision. It should be noted that in some cases a bubbler is not required if very dilute concentrations of the precursor are required. The only disadvantage of using a liquid precursor over gases is the added complexity of the vapour handling system.

The vapour delivery system for sublimable solid precursors is similar to liquid precursor delivery systems, specifically in its use of a carrier gas. Heating the solid precursor increases the sublimation rate. Sublimable solid precursors are the most difficult to handle for the following reasons. The sublimation rate of a solid is a function of temperature, the quantity of the solid precursor in the vessel and the carrier gas flow rate. Consequently, the delivery rate of precursor to the chamber can vary in the course of consecutive experiments unless the quantity and form of the starting material is the same at the beginning of each experiment. If care is taken, this is typically not a problem.

The most common difficulty encountered with the use of sublimable precursors is condensation onto the walls of the delivery lines and valves. Condensation occurs most often in the valve housings. This effect can be minimized by heating the gas lines and valves to a temperature above that of the precursor vessel.
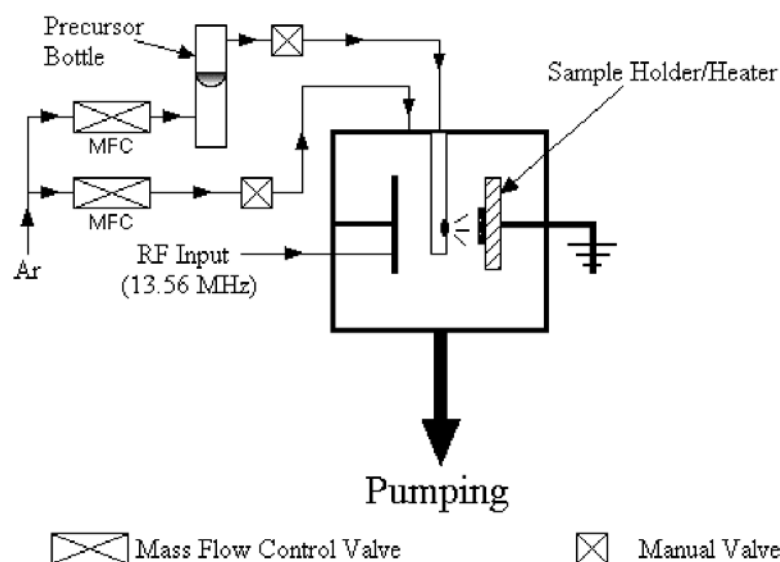
Figure 6. A schematic diagram of a parallel plate design of a plasma-enhanced chemical vapour deposition (PECVD) system used to synthesize nanowires.

A schematic of the plasma-enhanced chemical vapour deposition (PECVD) system in our laboratory is shown in figure 6. The system can be operated in either the CVD mode (plasma off) or the PECVD mode. The plasma is struck between two 3 inch diameter circular parallel plates (capacitor design) spaced approximately 1 inch apart. The sample is mounted on the grounded anode, which is also the sample heater. The sample heater is a boroelectric heater manufactured by GE Advanced Ceramics. The plasma frequency is the industry standard 13.56 MHz. The solid precursor *closo*-1,2-dicarbadodecaborane ($C_2B_{10}H_{12}$), which will be referred to from here on as orthocarborane, is used in the synthesis of boron carbide and silicon carbide nanowires and nanosprings. The system can be broken down into three subsystems: gas handling, reactor, and pumping system. The gas handling system consists of stainless steel tubing and metal gasket sealed fittings (VCR). The gas flow rates are controlled using mass flow control valves. The reactor consists of a six-way stainless steel cross with metal seal flanges. The system is pumped with a $300\,l\,s^{-1}$ diffusion pump backed by a mechanical pump. The achievable base pressure of the reactor is 5×10^{-5} Torr. A static pressure in the reactor is achieved by balancing the gas–vapour flow rates and the pumping speed, where regulation of the pumping speed is achieved by throttling the valve between the reactor and the diffusion pump.

3. Synthesis of nanowires

3.1. Boron carbide nanowires

The operating conditions of the plasma reactor in figure 6 are extremely important, where subtle variations can dramatically affect the composition and crystal structure of the nanowires. Typical operating conditions for growing boron carbide and silicon carbide nanowires and nanosprings are as follows. In all cases the substrate is Si, the source bottle containing orthocarborane is maintained at 60 °C, the plasma power is 50 W and the deposition time is 2 h. The specifics for BC or SiC nanowires are described in detail below. Regardless of nanowire composition, the 2 h deposition time produces, on average, nanowire lengths in excess of 5 μm.
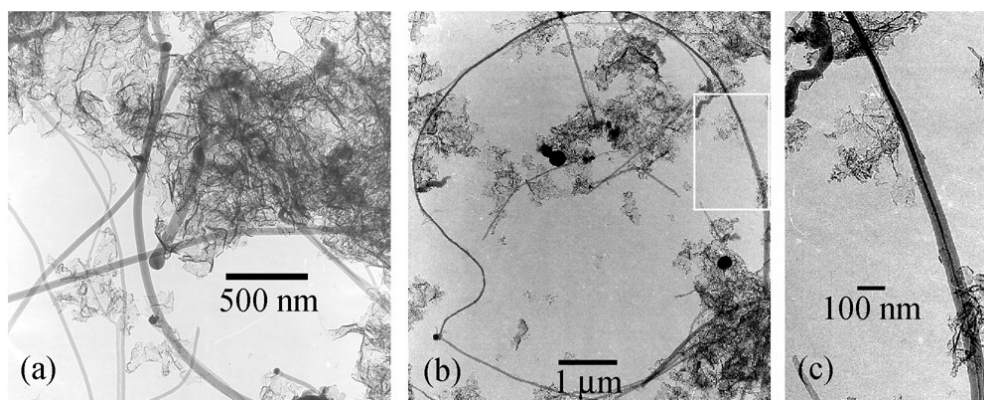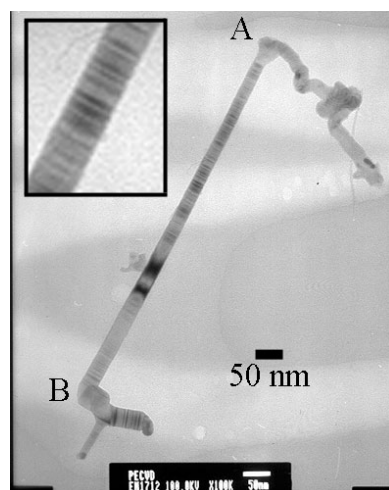
Figure 7. (a) A TEM image of a boron carbide nanowire, (b) a TEM image of a boron carbide nanowire tens of microns in length, and (c) a magnified image of the area in the white border of the evolution of the boron carbide nanowire from a biphase nanowire that is predominantly amorphous to a single-crystal nanowire.

In the PECVD process for synthesizing BC nanowires, FeB or NiB can be used as the catalyst and the substrate is maintained at a temperature ranging from 980 to 1100 °C. The Ar gas flow is 10 sccm directly into the PECVD chamber, while an additional 3 sccm of Ar passes through the source bottle into the chamber. The chamber pressure is maintained at 88 mTorr: 64 mTorr of Ar and 24 mTorr of orthocarborane/Ar. Examples of typical BC nanowire samples are shown in figure 7. The TEM image in figure 7(a) shows a number of BC nanowires, where the nanowire diameter distribution ranges from 17 to 67 nm, which is typically observed in all samples. The crystal structure of the BC nanowires is rhombohedral (hR15; space group $R3m$) in the B_4C phase [39, 41]. The growth is along the c-axis, or the [111] direction. The dark spherical caps at the end of a number of nanowires are the catalyst particles. Notice that the larger the catalyst, the larger the diameter of the corresponding nanowire, and that the diameter of the nanowire in the upper half of figure 7(b) is not constant but continuously evolves to a smaller diameter. This reflects the fact that the catalyst diameter dictates the maximum diameter of the ensuing nanowire, but not the minimum allowable diameter. It is also worth noting that the centre of mass of the catalyst is offset to one side of the nanowire axis. The significance of this on nanospring formation will become apparent later in the review. Figure 7(b) shows that extremely long BC nanowires of the order of tens of microns can be achieved.

A blow-up of the region bordered in white in figure 7(b) is (c). The difference in contrast between the centre and the edge of the BC nanowire indicates a biphase; the darker core is crystalline while the outer sheath is amorphous. The BC nanowire in panel (b) grows from right to left, which corresponds to nanowire growth from the bottom to the top of panel (c). Therefore, the crystalline core is growing while the amorphous sheath is thinning until the BC nanowire is entirely crystalline. This is significant since it illustrates that not only does the diameter of the nanowire change during formation, but that the evolution of the structure of the nanowire can also occur. Furthermore, if a nanowire can evolve from an amorphous structure to a crystalline structure, the opposite must also be true due to the coexistence of the two phases. In terms of nanospring formation, this is an extremely important point that will be addressed in detail in section 4.2.

3.2. Silicon carbide nanowires

In the PECVD process for synthesizing SiC nanowires, NiB is the catalyst and the Si substrate is maintained at a temperature ranging from 980 to 1100 °C. The Ar gas flow is 5 sccm directly

Figure 8. A TEM image of a complete silicon carbide nanowire. The inset in the upper left-hand corner is a magnified image showing stacking faults.

into the PECVD chamber, while an additional 1.5 sccm of Ar passes through the source bottle into the chamber. The chamber pressure is maintained at 122 mTorr: 98 mTorr of Ar and 24 mTorr of orthocarborane/Ar. Note that the Si source for synthesizing SiC nanowires is the Si substrate. We believe that the introduction of Si into the vapour is due to hydrogen etching, a byproduct of the dissociation of orthocarborane, as opposed to sublimation since the substrate temperature is well below the sublimation point of Si in high vacuum. The introduction of Si into the vapour is accompanied by a transformation of the catalyst from NiB to NiSi, which absorbs Si and C from the vapour, but not B. The only difference between this process and the process for synthesizing BC nanowires is the orthocarborane/Ar flow rate into the chamber. This translates into a lower orthocarborane partial pressure. This suggests that the partial pressure of orthocarborane is the determining factor in the assimilation of Si by the catalyst

Figure 8 is a TEM micrograph of a SiC nanowire: actually, there are two nanowires that originated from either of the points labelled A or B in figure 8. The crystalline structure of the SiC nanowires is cubic (β-SiC), with growth along the [111] direction. The striping is due to stacking faults, which are often observed for SiC nanowires [45, 68, 71]. If we assign A in figure 8 as the point of origin of nanowire growth, we see that the diameter increases linearly for the straight region of nanowire formation until an instability-induced bifurcation at B results in two nanowires, 11 and 33 nm in diameter, respectively. If B in figure 8 is chosen as the point of origin, then bifurcation initially occurs followed by nanowire growth. The origin of the instability that produced the bifurcation is probably a fluctuation in temperature during formation [83]. Another point worth noting in figure 8 is the erratic growth originating at A, which illustrates the extremely complex nature of nanowire formation, even within a single nanowire.

So-called biphase SiC nanowires, consisting of both crystalline and amorphous phases, are often observed. Examples of two such nanowires are shown in figure 9. The TEM image in figure 9(a) is a coaxial SiC nanowire, which consists of a β-SiC core and an amorphous SiC sheath. We believe that the two phases form simultaneously during nanowire growth rather than the sheath subsequently coating the crystalline core. In a previous study of coaxial SiC nanowires by Zhang *et al* [71], the core was found to be β-SiC while the shell was amorphous
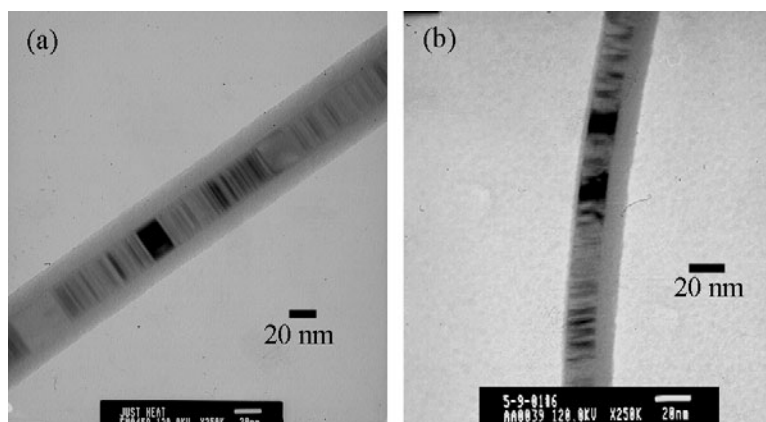
Figure 9. (a) A TEM micrograph of a biphase coaxial silicon nanowire consisting of a crystalline core and an amorphous sheath, and (b) a biphase silicon carbide nanowire where the amorphous material has grown predominantly on one side of the nanowire.

silica. The difference between the morphologies of the two forms of coaxial SiC nanowires arises from the different types of reactor and process employed. It is worth noting that coaxial nanowires have also been achieved through post-deposition of a sheath onto nanowires grown by the VLS mechanism [84]. The TEM image in figure 9(b) shows an asymmetric biphase SiC nanowire. The asymmetry suggests that the amorphous layer forms concomitant with the crystalline component. The details of biphase formation will be explored in greater detail when we examine the formation of coaxial helical nanowires in the following sections.
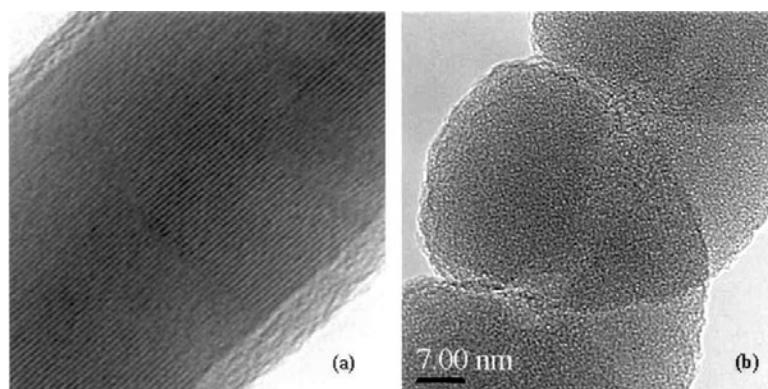
4. Nanosprings

4.1. Nanospring structure

The first observation of boron carbide nanosprings of the types in figure 10 was in a sample mostly composed of linear single-crystal nanowires. The diameters of the boron carbide nanosprings typically range from 20 to 30 nm, with pitches from 31 to 43 nm. The lengths of the nanosprings are typically 1–2 μm. The ratio of linear nanowires to nanosprings is approximately 10:1, although current research in our group is hoping to increase this ratio in a controlled manner. Studies of micron scale helical whiskers grown by VLS provided substantial insight into the development of our current understanding of how nanosprings form. Specifically, Motojima *et al* observed that the structures of the whiskers forming micron-scale springs of C [85] and Si_3N_4 [86], respectively, were amorphous. High resolution TEM was used to confirm that the boron carbide nanosprings were amorphous, rather than crystalline like their nanowire counterparts (figure 11) [70]. Well defined lattice planes are resolved for the boron carbide nanowire in figure 11(a), indicative of long range crystalline order, while no evidence of long range order is observed for the boron carbide nanospring in figure 11(b), indicative of the amorphous structure of the nanospring. These observations were also confirmed by electron diffraction.

Based on the results of Motojima *et al* and our studies, we have concluded that micron and nanoscale springs that grow via the VLS mechanism are only achievable when the structure of the whiskers or nanowires forming the springs are amorphous. The implication is that nanosprings of a wide range of compositions are possible. In support of this conclusion we have successfully synthesized silicon carbide nanosprings as shown in figure 12 [87]. Upon
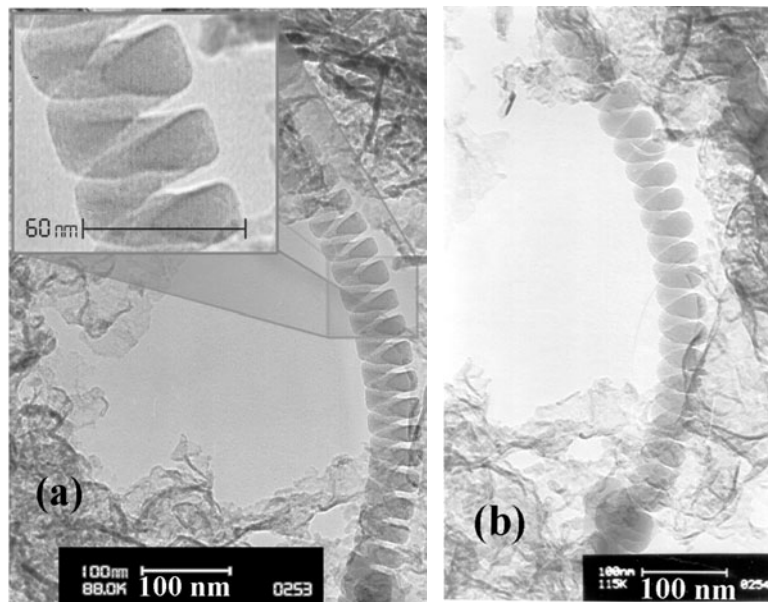
Figure 10. (a) A TEM image of a boron carbide nanospring [70] formed from a nanowire with a rectangular cross-section, and (b) a boron carbide nanospring formed from a nanowire with a circular cross-section.


Figure 11. (a) A high resolution TEM micrograph of a single-crystal boron carbide nanowire, and (b) a boron carbide nanospring formed from an amorphous boron carbide nanowire.

comparison of the silicon carbide nanosprings in figure 12 with the boron carbide nanosprings in figure 10, we see that they are very similar. The range of nanospring diameters, pitches, nanowire diameters, and overall length of the silicon carbide nanosprings are equivalent to those reported above for boron carbide nanosprings.

The cross-section of the boron carbide nanowire coiled into a nanospring in figure 10(a) is effectively rectangular, while the cross-sections of the boron carbide nanospring in figure 10(b) and the silicon carbide nanosprings in figure 12 are circular. An example of a silicon carbide nanospring having a rectangular cross-section is shown in figure 13. The ratio of the nanospring diameter to pitch is 1.9 for boron carbide in figure 10(a) and 2.0 for the silicon carbide in figure 13, which exhibit the squarest cross-sections for nanowires. The corresponding ratios
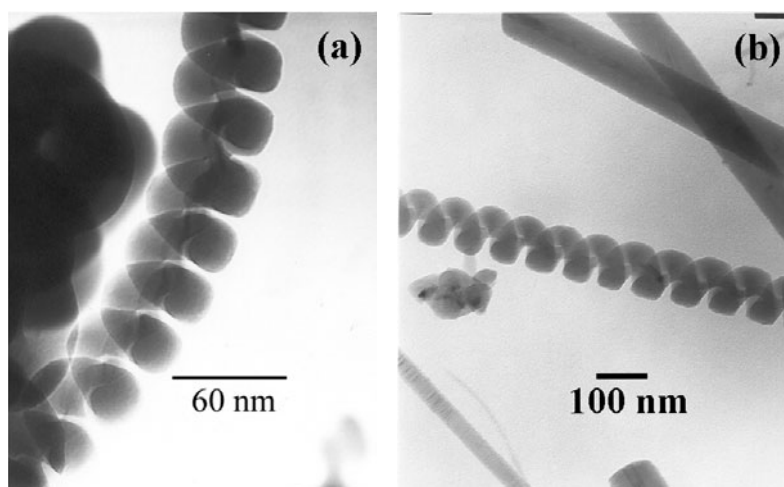
Figure 12. TEM images of a silicon carbide nanosprings formed from nanowires with circular cross-sections, where the nanospring diameter to pitch ratios are (a) 1.8 and (b) 1.23, respectively.

Figure 13. A TEM image of a silicon carbide nanospring formed from a nanowire with a rectangular cross-section, where the nanospring diameter to pitch ratio is 2.

for the silicon carbide nanosprings in figure 12, which have slightly less square nanowire cross-sections, are 1.8 and 1.23, respectively. The boron carbide nanospring in figure 10(b) has the smallest nanospring radius to pitch ratio at 0.85, as well as the roundest nanowire cross-section. We believe that the differences in nanospring cross-sections are due to differences in stress and strain during formation. We have found that larger ratios of nanospring diameter to pitch correlate with squarer nanowire cross-sections. We are currently exploring this issue and hope to demonstrate the validity of the above hypothesis.

4.2. Mechanism for nanospring formation

The helical structure of nanosprings is indicative of a highly asymmetric growth mode. In light of the evidence that nanosprings only form from amorphous nanowires [70, 71, 87], we can dismiss models based on lattice defects, such as screw dislocations. In fact, it was the lack of experimental evidence of screw dislocations in micron-scale crystalline whiskers that eventually led to the widespread acceptance of the VLS mechanism of whisker formation first proposed by Wagner and Ellis [72]. With this in mind, we have concluded that the anisotropy necessary for nanospring formation must originate from the catalyst during the growth process. In order to explain the formation of large pitch helical carbon nanotubes, Amelinckx *et al* [88] proposed that anisotropy of the velocity of the growth front, i.e., the carbon nanotube/catalyst interface, produced the necessary asymmetry. Unfortunately, the mechanism responsible for the anisotropic growth rate was not identified. Given that carbon nanotubes are ordered, the anisotropy could be a consequence of defects, which, in turn, affect the velocity of the growth front. However, an explanation of nanospring formation based on fluctuations of the defect densities at the growth front is incompatible with the amorphous structure of the nanosprings. Consequently, an alternative explanation of the origin of the growth anisotropy is necessary.

The catalyst dictates all aspects of nanowire formation, with the exception of the preferred growth direction of a crystalline nanowire. Consequently, anisotropy in the growth front of the forming nanosprings is linked to the catalyst composition and state. The growth rate of a nanowire is related to the rate at which material can diffuse from the surface of the catalyst to the catalyst/nanowire interface. However, the vapour composition and pressure about the catalyst should be fairly uniform; therefore, only temperature can affect the rate of adsorption onto the catalyst surface. Furthermore, any thermal asymmetry must also propagate through the catalyst from the nanowire interface.

The free energy of the interface can be described thermodynamically in terms of the surface tension previously discussed in section 2.1.2. The trajectory of the catalyst can be quantified by examining the work needed to shear the catalyst from the tip of the nanowire, which is related to the surface tensions (γ) between the liquid–vapour (γ_{LV}), solid–vapour (γ_{SV}), and solid–liquid (γ_{SL}) interfaces. The important quantities for the catalyst atop the nanowire in figure 14(a) are R, the radius of the droplet, ρ, the radius of the nanowire, and Δ, the displacement of the centre of mass of the catalyst from the central axis of the nanowire. Consider the two geometries of the catalyst in figure 4, as well as the corresponding surface tensions. These two geometries have azimuthal symmetry and therefore should result in linear nanowire growth. Now consider the geometry in figure 14(a), where the catalyst is offset from the axis of the nanowire. Note that this geometry is a hybrid of the two geometries in figure 4. At the interface labelled A in figure 14(a), the interfacial tensions γ_{LV} and γ_{SL} are antiparallel, while γ_{SV} is rotated by an angle θ out of the plane containing γ_{LV} and γ_{SL}. However, at interface B the interfacial tensions lie effectively within the same plane, where γ_{SV} is parallel to γ_{SL}. Consequently, there is a non-zero torque on the catalyst that will cause the catalyst to shear from the nanowire. We have therefore proposed that the growth asymmetry is due to a contact angle anisotropy (CAA) at the catalyst–nanowire interface, as depicted in figure 14(a), where CAA is a consequence of the displacement, Δ, of the catalyst.

The theoretical work required to disjoin the catalyst from the nanowire, referred to as the thermodynamic work of adhesion (W_A), can be quantified in terms of the interfacial energies [89] and is defined by the following relationship:

$$\begin{aligned} W_A &= \gamma_{SV} + \gamma_{SL} - \gamma_{LV} \\ &= \gamma_{SV} + \gamma_{SL} - (\gamma_{SL} + \gamma_{SV}\cos\theta) \\ &= \gamma_{SV}(1 - \cos\theta). \end{aligned} \tag{3}$$
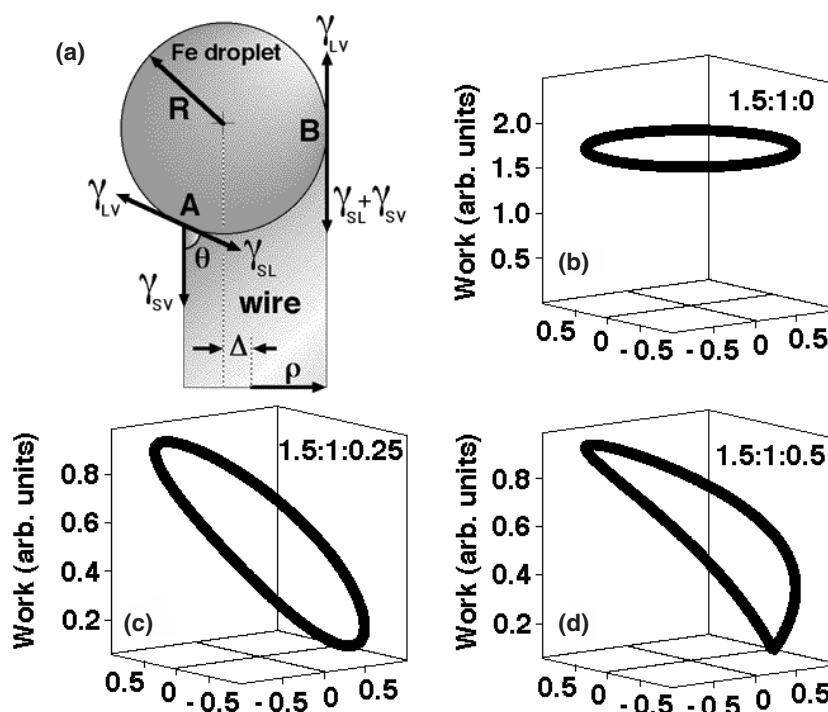
Figure 14. (a) A schematic diagram of a spherical catalyst located asymmetrically atop of a nanowire and the corresponding surface tensions, (b) the work of adhesion of a spherical catalyst located symmetrically atop a nanowire, (c) slightly off the axis of the nanowire, and (d) for the geometry depicted in (a) [70].

Consequently, the work of adhesion depends on the angle between γ_{SV} and γ_{SL}. At interface A (figure 14(a)) the interaction between the droplet and the nanowire is a nonwetting interaction, while at interface B the droplet is in a condition of spontaneous wetting, i.e. $\theta = 0$.

The work of adhesion as calculated from the surface energies at the perimeter of the droplet–wire interface for a number of geometries are shown in figures 14(b)–(d). For all of the calculations we have chosen the ratio of the droplet radius (R) to the nanowire radius (ρ) to be 1.5, which is the average value observed for spherical catalysts. If the centre of mass of the droplet coincides with the central axis of the nanowire, the work of adhesion (figure 14(b)) is uniform about the perimeter of the droplet/nanowire interface and therefore precludes asymmetric growth, i.e., helical growth. However, by offsetting the droplet from the axis of the nanowire, CAA is introduced and W_A (figure 14(c)) is no longer symmetric, where the minimum corresponds to the closest approach of the interface to the edge of the droplet. In figure 14(d) W_A has been plotted for the conditions depicted in figure 14(a), where the offset has been increased to half of the radius of the nanowire, thereby maximizing CAA. In addition to the expected asymmetry, a well defined cusp in W_A is introduced at interface B (figure 14(a)). Note that by systematically increasing the radius of the droplet the CAA will become insignificant and the work of adhesion will be essentially symmetric.

The significance of the asymmetry in the work of adhesion in figure 14(d) is as follows. The probability of an atom diffusing through the catalyst and attaching itself to a point at the droplet–nanowire interface will be a function of the energy needed to break a droplet–nanowire bond, less the energy gained by making a bond to the nanowire, whether chemical or physical.
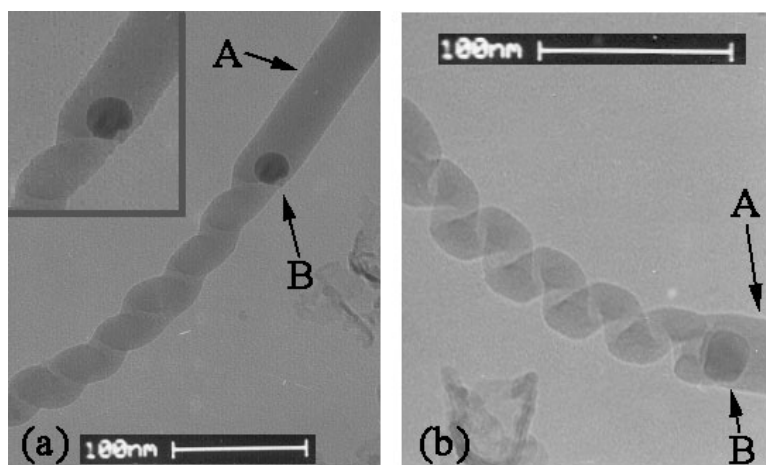
Figure 15. TEM images of the transitions from linear nanowire growth to nanospring growth [70]. The dark regions at the transitions are due to iron boride nanoparticles (catalyst).

The probability of attachment of an atom at the droplet–nanowire interface is greater for interfacial locations with lower W_A. In other words, the adsorption energy of a precursor atom or molecule is expected to be higher, that is, more exothermic and/or entropically favoured, than the adsorption energy of the catalyst. So, the growth rate at interface B (v_B) will be greater than the growth rate at interface A (v_A), thereby creating the asymmetry necessary to curl the trajectory of the droplet back upon the nanowire. In doing so, this will distort the wetted area from its original circular shape into an ellipse, as the cross-section of a cylinder taken at an angle other than perpendicular to the main axis. The catalyst drop will be forced into an oblate form with the increasing eccentricity of the wetted perimeter. The total surface energy can no longer be minimized and at some point the stretched catalyst will split, as discussed below for the helical transition. Because the cusp in figure 14(d) is a point of instability, a small lateral perturbation will produce the precession necessary to drive the droplet into a spiral trajectory that can be described using the trajectory mechanics of Amelinckx *et al* [88] for helical carbon nanotubes. Based on the analysis of the work of adhesion of the catalyst to the nanowire, we have concluded that the optimal geometry for promoting spiral growth is achieved when the ratio $R/\rho \simeq 1.5$ and the extreme edge of the droplet coincides with the edge of the nanowire, as depicted in figure 14(a).

The transition from linear to helical growth of two boron carbide nanowires/nanosprings is shown in figure 15. The arrows in figure 15 identify remnants of the catalyst that have become lodged at the transition points; the remaining portions of the catalysts continue on at the tip of the nanospring. Similar observations by Zhang *et al* [90] for SiO_2 nanosprings have been reported. Catalyst bifurcation has been experimentally induced in micron scale whiskers [83]. Consequently, we have concluded that temperature fluctuations during nanowire formation perturb the growth process, thereby inducing the transition from linear to helical growth. The diameters of the ejected Fe droplets can be calculated from the dimensions of the straight nanowires and the helical nanowires in figure 15. First, we assume that the diameter of the parent droplet was equivalent to the diameter of the straight wire. Second, we assume a spherical geometry for the ejected droplet, which is supported by the observed spherical shape of the encased Fe droplets in figure 15 and by TEM images of straight BC nanowires capped with spherical Fe particles. Therefore, the diameters of the ejected Fe droplets that formed the

Figure 16. A TEM image of a biphase helical nanowire, which consists of a helical silicon carbide crystalline core and an amorphous silicon carbide sheath [87]. The dark region at the tip of the nanowire is the nickel silicide catalyst.

nanosprings were 19 nm (figure 15 (a)) and 17 nm (figure 15(b)), respectively. The ratios of the radii of the ejected droplets (R) to the radii of the nanowires (ρ) forming the nanosprings are 1.36 (figure 15(a)) and 1.54 (figure 15 (b)), respectively. These values are in excellent agreement with the optimal R/ρ ratio of 1.5, as determined from the CAA model.

The observed growth of amorphous boron carbide nanosprings, in conjunction with the CAA model, illustrates the importance of the catalyst for promoting nanowire growth, as well as the effect of its trajectory on geometry. Furthermore, since the CAA model for nanospring growth is material independent, provided the wires are amorphous, it can be universally used to describe the growth of all types of nano- and micron-sized springs, regardless of their composition. This conclusion is supported by the observation of silicon carbide [87] and silicon dioxide [90] nanosprings formed from amorphous nanowires. The accessibility of this technique for synthesizing nanosprings, namely, that the only two requirements are that the nanowires be amorphous and grow via the VLS mechanism, suggests that the mechanical properties of nanosprings can be tuned through control of their physical dimensions and the type of material from which the nanosprings are formed.

5. Crystalline core/amorphous shell helical nanowires

Helical nanowires consisting of a crystalline SiC core encased in an amorphous shell SiO$_2$ were first observed by Zhang *et al* [71]. Similarly, our group has reported crystalline core helical nanowires consisting of SiC encased in an amorphous SiC shell (figure 16) [87]. A screw dislocation model was proposed by Zhang *et al* [71] to explain the formation of their biphase helical nanowires. While a screw dislocation model offers an attractive explanation of how unique nanostructures form, the historical record of whisker research does not support the existence of screw dislocations in micron or nanoscale wires [91]. Furthermore, no evidence of screw dislocations in these crystalline core helical nanowires has been presented. We have suggested instead that it is the difference in the growth rates of the two phases that is responsible for the formation of these unique morphologies [87].

The significance of the amorphous shell to the formation of the helical crystalline core of the nanowire in figure 16 is clarified through the application of the CAA model. Specifically, by analysing the degrees of anisotropy at the interfaces between the catalyst and the amorphous shell and the catalyst and the crystalline core, we can evaluate the magnitudes of their contributions to the net interfacial anisotropy. In figure 16, the diameter of the catalyst (d_{catalyst}) is 68.4 nm, the diameter of the amorphous shell ($d_{\alpha\text{-shell}}$) is 52.6 nm, and the diameter of the crystalline core ($d_{\text{c-core}}$) is 10.5 nm, respectively. By offsetting the catalyst from the axis of the nanowire, anisotropy at the point of contact between the catalyst and the nanowire is introduced and the work of adhesion W of the catalyst to the nanowire is no longer symmetric. The work of adhesion anisotropy (α_W) can be expressed by the following:

$$\alpha_W = \frac{W_{\text{max}} - W_{\text{min}}}{W_{\text{max}}} = \frac{\Delta W}{W_{\text{max}}}. \tag{4}$$

Using diameters normalized to that of the amorphous shell ($d_{\alpha\text{-shell}}$), we have $d_{\text{catalyst}}:d_{\alpha\text{-shell}}:d_{\text{c-core}} = 1.3:1:0.2$ and an offset between the catalyst and α-shell nanowire ($\Delta_{\text{catalyst}/\alpha\text{-shell}}$) of 0.30 (with this offset, the edge of the amorphous shell of the nanowire is aligned with the edge of the catalyst). For this geometry, the maxima of the works of adhesion (as unitless relative values) at the catalyst/α-shell nanowire interface are

$$W_{\text{max}} = 1.8427 \times 10^{-2} \qquad \text{and} \qquad W_{\text{min}} = 1.0074 \times 10^{-2},$$
$$\text{with } \Delta W = 8.353 \times 10^{-3}.$$

Upon insertion of these values into equation (4), the anisotropy in the works of adhesion for the amorphous shell $\alpha_{W_{\alpha\text{-shell}}}$ is

$$\alpha_{W_{\alpha\text{-shell}}} = \frac{\Delta W}{W_{\text{max}}} = 0.45.$$

In order to evaluate α_W at the catalyst/crystalline core interface, an offset between the catalyst and the crystalline core ($\Delta_{\text{catalyst}/\text{c-core}}$) of 1.5 has been used, which is based on the offset used above for the amorphous shell. The offset for the crystalline core can range from zero to a maximum of 5.5 in normalized dimensions. For an offset of 1.5, the maxima of the works of adhesion for the catalyst/crystalline core interface are

$$W_{\text{max}} = 1.997 \times 10^{-2} \qquad \text{and} \qquad W_{\text{min}} = 1.923 \times 10^{-2},$$
$$\text{with } \Delta W = 7.4 \times 10^{-4}.$$

The corresponding anisotropy in the work of adhesion for the crystalline core $\alpha_{W_{\text{c-core}}}$ is

$$\alpha_{W_{\text{c-core}}} = \frac{\Delta W}{W_{\text{max}}} = 0.037.$$

The anisotropy in the work of adhesion is clearly dominated by that of the amorphous shell ($\alpha_{W_{\alpha\text{-shell}}} = 0.45$) relative to that of the crystalline core ($\alpha_{W_{\text{c-core}}} \sim 0.04$). Furthermore, the anisotropy for the amorphous SiC shell is comparable to that calculated for amorphous BC nanosprings (0.44) [70]. From the standpoint of the anisotropy in the works of adhesion of the catalyst to the nanowire, the contribution of the crystalline core is small; however, we believe that the magnitude of the work of adhesion between the crystalline core and the nanowire is not insignificant. In fact, we propose that the crystalline core effectively pins the catalyst, thereby prohibiting nanospring formation of the type in figure 10, in favour of helical biphase formation in figure 16.

In support of the above conclusion, we present in figure 17 a TEM micrograph of the transition from linear to nanospring-like growth of a crystalline core/amorphous shell nanowire. Note that the transition to nanospring-like growth corresponds to the extinction of the crystalline
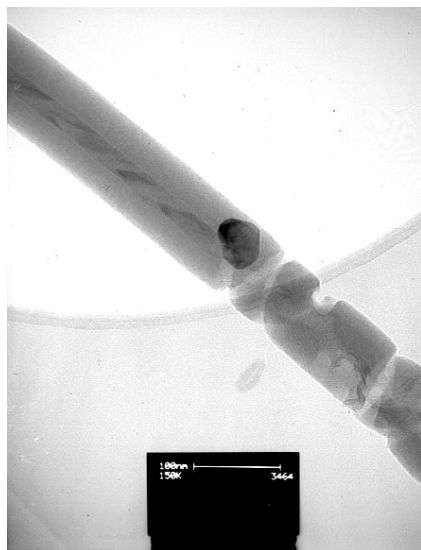
Figure 17. A TEM image of the transition region from linear to nanospring growth of a biphase amorphous shell/crystalline core silicon carbide nanowire [87].

core, thereby eliminating the pinning of the catalyst. Once again, a portion of the catalyst remains at the transition, which is consistent with earlier observations. The pinning of the catalyst by the crystalline core is probably a consequence of the fact that nanowire formation is preferential, i.e., the growth direction is along a well defined crystallographic direction. This direction is often perpendicular to the surface with the minimum free energy—the free energy of the wall of the nanowire should also be taken into account. The net result is that it is energetically unfavourable for the crystalline core to grow in a direction other than that leading to minimization of the free energy. Consequently, the anisotropy introduced by the amorphous shell only acts as a perturbation during the growth process, with the end result being helical nanowires of the type in figure 16. The pitch of the amorphous shell/crystalline core helixes is probably dictated by the maximum allowable rotation and/or translation vector between adjacent crystal planes. Once again, only with the extinction of the crystalline core can nanosprings of the type in figures 10 and 12 be achieved.

6. Mechanical properties of nanosprings

Due to the extremely small size of nanosprings ($<$100 nm), measurements of their mechanical properties have proven to be challenging. Our initial experiments to measure the mechanical properties of boron carbide nanosprings involved simultaneously heating the support grid containing the nanosprings while observing them in a TEM. The rationale for heating was to induce vibrations, i.e., transverse deflections, in the nanosprings. From the magnitude of the transverse oscillations of the nanospring, be it fixed at one end or both ends, the fundamental properties such as the Young's modulus, etc, can be extracted. While straightforward, changes in the properties of materials once their dimensions approach the nanoscale, specifically the reduction in their melting or re-crystallization temperature, have not been appreciated. To illustrate this point we show a TEM image in figure 18 of a boron carbide nanospring at room temperature (a) and at 300 °C (b). Upon comparing the boron carbide nanospring before and
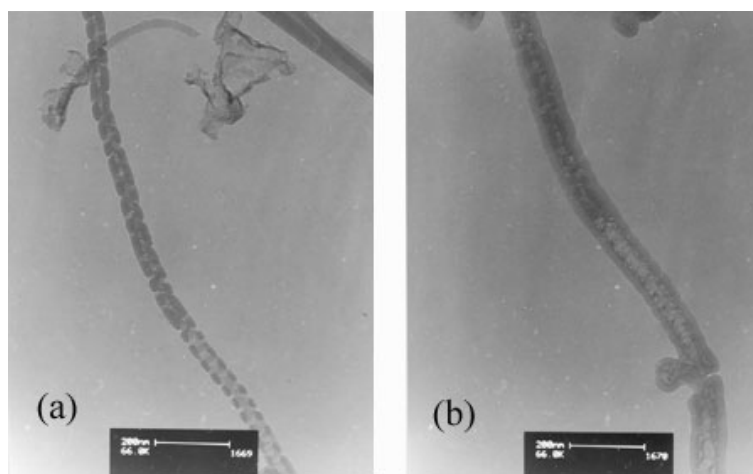
Figure 18. (a) A TEM image of a boron carbide nanospring at room temperature and (b) the same spring heated to 300 °C.

after mild heating we see that neighbouring coils have coalesced, thereby destroying the spring geometry and eliminating any chances of measuring the spring's nanomechanical properties. We have attributed the deformation of the nanospring to a reduction in the crystallization temperature of amorphous boron carbide from above 1000 °C to approximately 300 °C. Almost complete crystallization of the boron carbide nanospring was achieved at 800 °C. As a consequence of the results these experiments were abandoned; however, these experiments are being pursued with SiC nanosprings, with the hope that crystallization of the SiC nanospring does not occur. The outcome of these forthcoming experiments may shed valuable light on the mechanical properties of nanosprings, as well as the properties of amorphous materials at the nanoscale.

The first demonstration of springlike behaviour was by Zhang *et al* [90] for silicon dioxide nanosprings. In this study the mechanical properties of SiO_2 nanosprings were not measured directly, but some interesting results were obtained. The experiment consisted of heating a section of the nanospring with a focused electron beam (e-beam heating) in a TEM. In this experiment they demonstrated that a segment of the nanospring could be elongated with heating. The elongation was accompanied by a contraction of the nanospring in an adjacent segment, which suggests that heating reduces the local spring constant. The corresponding elongation and contraction is a redistribution of force along the nanospring in order to equilibrate, or reach a static mechanical condition. Subsequent e-beam heating of the contracted segment of the nanospring led to elongation, which supports the suggestion that e-beam heating reduces the spring constant. This study went on to demonstrate that the SiO_2 nanosprings could be deflected with the tip of an atomic force microscope (AFM). This study did not obtain quantitative measurements of the nanospring mechanical properties.

A subsequent study of micron scale carbon coils by Chen *et al* [92] successfully extracted quantitative mechanical results. In this study, 2 μm diameter carbon coils were elongated between two AFM tips, which could be imaged simultaneously with a scanning electron microscope. Quantitatively, a linear dependence of load (μN) as a function of elongation of the order of a few microns was demonstrated, where the pitch of the coil was approximately 1 μm. To date, this is the only study the authors are aware of where a direct mechanical measurement of a micron-scale spring has been achieved. This study by Chen *et al* [92] is very

encouraging, yet the quantitative measurement of the mechanical properties of nanosprings in the size regime of those in figures 10 and 12 will be significantly more challenging.

More exotic indirect measurements, such as electromechanical response, may be more feasible for measuring the mechanical properties of nanosprings. One possible experiment is to pass current through a nanospring, where the Lorentz force between adjacent coils will cause the spring to contract, thereby changing the inductance of the nanospring. Such a response could easily be measured, and in turn used to calculate the mechanical properties. While challenging, this type of experiment may be a better method for accurately measuring nanospring mechanical properties. Furthermore, the successful completion of this type of experiment would open up a vast number of applications for nanosprings as electromechanical devices and sensors.

7. Concluding remarks

While nanomechanics is not new *per se*, most of the nanomechanical problems studied are irreversible and/or indirect, such as grain boundary slippage and the like. In the case of nanosprings, we have the opportunity to study a dynamic system. Consequently, future studies of the mechanical properties of nanosprings will shed new insight on the effects of stress and strain on the mechanical integrity of nanoscale structures. However, because of the immaturity of the field, very little is known about their mechanical properties, let alone their electromechanical response. Fortunately, we know how nanosprings form and, therefore, the availability of nanosprings for study will grow. The need to develop exotic electromechanical experiments in order to study their mechanical properties will simultaneously illuminate their potential application as nanoscale devices and sensors. The future of nanomaterials is wide open, yet we will need to rethink how machines at the nanoscale should be constructed. While machines, as we know them in our everyday lives, are impractical at the nanoscale, energy at the nanoscale will still be an important commodity. In the not too distant future nanosprings may prove to be an integral part of the power plant for nanomachines of tomorrow.

Acknowledgment

References

[1] Moore G E 1965 *Electronics* **38** 114–7
[2] Osuna J, de Caro D, Amiens C, Chaudret B, Snoeck E, Respaud M, Broto J-M and Fert A 1996 *J. Phys. Chem.* **100** 14571
[3] Sun Y, Gates B, Mayers B and Xia Y 2002 *Nano Lett.* **2** 165
[4] Vossmeyer T, Katsikas L, Giersig M, Popovic I G, Diesner K, Chemseddine A, Eychmuller A and Weller H 1994 *J. Phys. Chem.* **98** 7665
[5] Goglio G, Pignard S, Radulescu A, Piraux L, Huynen I, Vanhoenacker D and Vander Vorst A 1999 *Appl. Phys. Lett.* **75** 1769
[6] Huber T E and Graf M J 1999 *Phys. Rev.* B **60** 16880
[7] Kovtyukhova N I, Martin B R, Mbindyo J K N, Smith P A, Razavi B, Mayer T S and Mallouk T E 2001 *J. Phys. Chem.* B **105** 8762
[8] Duan X and Lieber C M 2000 *J. Am. Chem. Soc.* **122** 188
[9] Tang C C, Fan S S, Dang H Y, Li P and Liu Y M 2000 *Appl. Phys. Lett.* **77** 1961

[10] Peng H Y, Zhou X T, Wang N, Zheng Y F, Liao L S, Shi W S, Lee C S and Lee S T 2000 *Chem. Phys. Lett.* **327** 263

[11] He M, Minus I, Zhou P, Mohammed S N, Jacobs R, Sarney W L, Salamanca-Riba L and Vispute R D 2000 *Appl. Phys. Lett.* **77** 3731

[12] Huo K F, Hu Z, Chen F, Fu J J, Chen Y, Liu B H, Ding J, Dong Z L and White T 2002 *Appl. Phys. Lett.* **80** 3611

[13] Seo H W, Bae S Y, Park J, Yang H, Park K S and Kim S 2002 *J. Chem. Phys.* **116** 9492

[14] Liang C H, Chen L C, Hwang J S, Chen K H, Hung Y T and Chen Y F 2002 *Appl. Phys. Lett.* **81** 22

[15] Huang M H, Wu Y, Feick H, Tran N, Weber E and Yang P 2001 *Adv. Mater.* **13** 113

[16] Kong Y C, Yu D P, Zhang B, Fang W and Feng S Q 2001 *Appl. Phys. Lett.* **78** 407

[17] Pan Z W, Dai Z R and Wang Z L 2001 *Science* **291** 1947

[18] Yazawa M, Koguchi M and Hiruma K 1991 *Appl. Phys. Lett.* **58** 1080

[19] Duan X and Lieber C M 2000 *Adv. Mater.* **12** 298

[20] Gudiksen M S and Lieber C M 2000 *J. Am. Chem. Soc.* **122** 8801

[21] Gudiksen M S, Wang J and Lieber C M 2001 *J. Phys. Chem.* B **105** 4062

[22] Morales A M and Lieber C M 1998 *Science* **279** 208

[23] Ozaki N, Ohno Y and Takeda S 1998 *Appl. Phys. Lett.* **73** 3700

[24] Au F C K, Wong K W, Tang Y H, Zhang Y F, Bello I and Lee S T 1999 *Appl. Phys. Lett.* **75** 1700

[25] Tang Y H, Zhang Y F, Wang N, Lee C S, Han X D, Bello I and Lee S T 1999 *J. Appl. Phys.* **85** 7981

[26] Ozaki N, Ohno Y and Takeda S 1998 *Appl. Phys. Lett.* **73** 3700

[27] Zhang Y F, Tang Y H, Peng H Y, Wang N, Lee C S, Bello I and Lee S T 1999 *Appl. Phys. Lett.* **75** 1842

[28] Wang R-P, Zhou G-W, Long Y L, Pan S-H, Zhang H-Z, Yu D-P and Zhang Z 2000 *Phys. Rev.* B **61** 16827

[29] Gu Q, Dang H, Cao J, Zhao J and Fan S 2000 *Appl. Phys. Lett.* **76** 3020

[30] Kamins T I, Williams R S, Basile D P, Hesjedal T and Harris J S 2001 *J. Appl. Phys.* **89** 1008

[31] Sun X H, Peng H Y, Tang Y H, Shi W S, Wong N B, Lee C S, Lee S T and Sham T K 2001 *J. Appl. Phys.* **89** 6396

[32] Cui Y, Lauhon L J, Gudiksen M S, Wang J and Lieber C M 2001 *Appl. Phys. Lett.* **78** 2214

[33] Sunkara M K, Sharma S, Miranda R, Lian G and Dickey E C 2001 *Appl. Phys. Lett.* **79** 1546

[34] Peng H Y, Wang N, Shi W S, Zhang Y F, Lee C S and Lee S T 2001 *J. Appl. Phys.* **89** 727

[35] Peng H Y, Pan Z W, Xu L, Fan X H, Wang N, Lee C S and Lee S T 2001 *Adv. Mater.* **13** 317

[36] Tang Y H, Sham T K, Jürgensen A, Hu Y F, Lee C S and Lee S T 2002 *Appl. Phys. Lett.* **80** 3709

[37] Barsotti R J Jr, Fischer J E, Lee C H, Mahmood J, Adu C K W and Eklund P C 2002 *Appl. Phys. Lett.* **81** 2866

[38] Dikin D A, Chen X, Ding W, Wagner G and Ruoff R S 2003 *J. Appl. Phys.* **93** 226

[39] Zhang D, McIlroy D N, Geng Y and Norton M G 1999 *J. Mater. Sci. Lett.* **18** 349

[40] Zhou X T, Wang N, Lai H L, Peng H Y, Bello I, Wong N B, Lee C S and Lee S T 1999 *Appl. Phys. Lett.* **74** 3942

[41] McIlroy D N, Zhang D, Cohen R M, Wharton J, Geng Y, Norton M G, De Stasio G, Gilbert B, Perfetti L, Streiff J H, Broocks B and McHale J L 1999 *Phys. Rev.* B **60** 4874

[42] Wong K W, Zhou X T, Au F C K, Lai H L, Lee C S and Lee S T 1999 *Appl. Phys. Lett.* **75** 2918

[43] Hu J Q, Lu Q Y, Tang K B, Deng B, Jiang R R, Qian Y T, Yu W C, Zhou G E, Liu X M and Wu J X 2000 *J. Phys. Chem.* B **104** 5251

[44] Liang C H, Meng G W, Zhang L D, Wu Y C and Cui Z 2000 *Chem. Phys. Lett.* **329** 323

[45] Lai H L, Wong N B, Zhou X T, Peng H Y, Au F C K, Wang N, Bello I, Lee C S, Lee S T and Duan X F 2000 *Appl. Phys. Lett.* **76** 294

[46] Zhang H-F, Dohnalkova A C, Wang C-M, Young J S, Buck E C and Wang L S 2002 *Nano Lett.* **2** 105

[47] Wu Z S, Deng S Z, Xu N S, Chen J, Zhou J and Chen J 2002 *Appl. Phys. Lett.* **80** 3829

[48] Gundiah G, Madhav G V, Govindaraj A, Seikh Md M and Rao C N R 2002 *J. Mater. Chem.* **12** 1606

[49] Liang C H, Meng G W, Wang G Z, Wang Y W, Zhang L D and Zhang S Y 2001 *Appl. Phys. Lett.* **78** 3202

[50] Zhu D, Zhu H and Zhang Y 2002 *Appl. Phys. Lett.* **80** 1634

[51] Hu J, Ouyang M, Yang P and Lieber C M 1999 *Nature* **399** 48

[52] Duan X, Huang Y, Cui Y, Wang J and Lieber C M 2001 *Nature* **409** 66

[53] Cui Y and Lieber C M 2001 *Science* **291** 851

[54] Huang Y, Duan X, Cui Y, Lauhon L J, Kim K-H and Lieber C M 2001 *Science* **294** 1313

[55] Gudiksen M S, Lauhon L J, Wang J, Smith D C and Lieber C M 2002 *Nature* **415** 617

[56] Huang Y, Duan X, Cui Y and Lieber C M 2002 *Nano Lett.* **2** 101

[57] Cui Y, Wei Q, Park H and Lieber C M 2001 *Science* **293** 1289

[58] Duan X, Huang Y and Lieber C M 2002 *Nano Lett.* **2** 487

[59] Duan X, Wang J and Lieber C M 2000 *Appl. Phys. Lett.* **76** 1116

[60] Zheng M J, Zhang L D, Li G H, Zhang X Y and Wang X F 2001 *Appl. Phys. Lett.* **79** 839

[61] Wang J, Gudiksen M S, Duan X, Cui Y and Lieber C M 2001 *Science* **293** 1455
[62] Gudiksen M S, Wang J and Lieber C M 2002 *J. Phys. Chem.* B **106** 4036
[63] Tang Z, Kotov N A and Giersig M 2002 *Science* **297** 237
[64] Mock J J, Oldenburg S J, Smith D R, Schultz D A and Schultz S 2002 *Nano Lett.* **2** 465
[65] Wu Y, Fan R and Yang P 2002 *Nano Lett.* **2** 83
[66] Bjork M T, Ohlsson B J, Sass T, Persson A I, Thelander C, Magnusson M H, Deppert K, Wallenberg L R and
        Samuelson L 2002 *Nano Lett.* **2** 87
[67] Wang Z L, Dai Z R, Gao R P, Bai Z G and Gole J L 2000 *Appl. Phys. Lett.* **77** 3349
[68] Tang C C, Bando Y, Sato T, Kurashima K, Ding X X, Gan Z W and Qi S R 2002 *Appl. Phys. Lett.* **80** 4641
[69] Tang Y H, Zhang Y F, Wang N, Lee C S, Han X D, Bello I and Lee S T 1999 *J. Appl. Phys.* **85** 7981
[70] McIlroy D N, Zhang D, Kranov Y and Norton M G 2001 *Appl. Phys. Lett.* **79** 1540
[71] Zhang H-F, Wang C-M and Wang L-S 2002 *Nano Lett.* **2** 941
[72] Wagner R S and Ellis W C 1964 *Appl. Phys. Lett.* **4** 89
[73] See for example Massalski T B (ed) 1986 *Binary Alloy Phase Diagrams* (Metals Park, OH: ASM International)
[74] Coombes C J 1972 *J. Phys. F: Met. Phys.* **2** 441
[75] Castro T, Reifenberger R, Choi E and Andres R P 1990 *Phys. Rev.* B **42** 8548
[76] Goldstein A N, Echer C M and Alivisatos A P 1992 *Science* **256** 1425
[77] Nanda K K, Kruis F E and Fissan H 2002 *Phys. Rev. Lett.* **89** 256103
[78] McIlroy D N, Zhang D, Kranov Y, Han H, Alkhateeb A and Norton M G 2003 *Mat. Res. Sym. Proc.* **739** 164
[79] Jackson K A and Wagner R S 1965 *J. Appl. Phys.* **36** 2132
[80] Levitt A B (ed) 1970 *Whisker Technology* (New York: Wiley–Interscience) p 63
[81] Israelachvili J N 1992 *Intermolecular and Surface Forces* 2nd edn (London: Harcourt Brace) chapter 15
        (Adhesion)
[82] Levitt A B (ed) 1970 *Whisker Technology* (New York: Wiley–Interscience) p 249
[83] Levitt A B (ed) 1970 *Whisker Technology* (New York: Wiley–Interscience) p 109
[84] Lauhon L J, Gudiksen M S, Wang D and Lieber C M 2002 *Nature* **420** 57
[85] Motojima S, Ueno S, Hattori T and Goto K 1989 *Appl. Phys. Lett.* **54** 1001
[86] Motojima S, Kawaguchi M, Nozaki K and Iwanaga H 1990 *Appl. Phys. Lett.* **56** 321
[87] Zhang D, Alkhateeb A, Han H, Mahmood H, McIlroy D N and Norton M G 2003 *Nano Lett.* **3** 983
[88] Amelinckx S, Zhang X B, Bernaerts D, Zhang X F, Ivanov V and Nagy J B 1994 *Science* **265** 635
[89] Levitt A B (ed) 1970 *Whisker Technology* (New York: Wiley–Interscience) p 257
[90] Zhang H-F, Wang C-M, Buck E C and Wang L-S 2003 *Nano Lett.* **3** 577
[91] Levitt A B (ed) 1970 *Whisker Technology* (New York: Wiley–Interscience) p 57
[92] Chen X, Zhang S, Dikin D A, Ding W, Ruoff R S, Pan L and Nakayamy Y 2003 *Nano Lett.* **3** 1299